processes

MDPI

Article

Pore Distribution Characteristics of Different Lithofacies Shales: Evidence from Scanning Electron Microscopy

Junjie Wang [1], Shuangfang Lu [2], Pengfei Zhang [3,*], Qi Zhi [1] and Hongsheng Huang [1]

[1] School of Geosciences, China University of Petroleum (East China), Qingdao 266580, China; wjj19990125@163.com (J.W.)
[2] Sanya Offshore Oil & Gas Research Institute, Northeast Petroleum University, Sanya 572025, China
[3] College of Earth Science and Engineering, Shandong University of Science and Technology, Qingdao 266590, China
* Correspondence: zhangpengfei0907@sdust.edu.cn

Abstract: To disclose the pore distribution characteristics of different lithofacies lacustrine shales, ten samples collected from the Shahejie Formation, Dongying Sag, Bohai Bay Basin, China, were examined using argon ion beam milling–scanning electron microscopy (SEM). A quantitative method was adopted to characterize shale pore distributions based on the SEM images. Mercury intrusion capillary pressure was employed to determine the pore throat size distributions of the shales. The SEM images indicated that in shale reservoirs, interparticle pores at the edges of brittle particles and intraparticle pores in clay mineral aggregates primarily contribute to the reservoir spaces and that in calcite-rich shales, dissolution pores provide secondary reservoir space. Among the morphologies of dissolution, intraparticle, and interparticle pores, the morphology of the dissolution pores is the simplest, followed by those of intraparticle and interparticle pores in that order. Clay and felsic minerals primarily control the shale pore sizes and the larger the clay mineral content in the shales, the smaller their pore size; the felsic minerals demonstrate the opposite behavior. The image-based point counting data indicate that shale pore sizes are mostly between 20 nm and 2 μm. In contrast, most pore throats are less than 20 nm in diameter, implying that the pores in the nanometer to micrometer scales are connected by tiny throats. Among the four lithofacies shales, felsic-rich shales are favorable for shale oil accumulation and seepage because of their large pore sizes and throats their ability to form intercalated shale oil adjacent to organic-rich shales. Calcareous shales with a large number of dissolution pores and a large content of organic matter could produce self-generation and self-storage matrix shale oil and would typically develop fractures, thereby creating a seepage channel for shale oil. This study presents the micro-distributions of different lithofacies of shale pores, which would help in understanding the occurrence and seepage of oil in shale reservoirs.

Keywords: pore size; pore morphology; lacustrine shale; scanning electron microscopy; Dongying Sag

Citation: Wang, J.; Lu, S.; Zhang, P.; Zhi, Q.; Huang, H. Pore Distribution Characteristics of Different Lithofacies Shales: Evidence from Scanning Electron Microscopy. *Processes* **2023**, *11*, 1120. https://doi.org/10.3390/pr11041120

Academic Editor: Qingbang Meng

Received: 16 March 2023
Revised: 27 March 2023
Accepted: 3 April 2023
Published: 5 April 2023

1. Introduction

Shale oil is the mature oil occurring in the shale series. Owing to the substantial resources, shale oil has been concerned and succeeded in North America [1]. Under the context of carbon neutralization, shale oil exploitation is not a clean way. With the development of technologies of carbon capture, utilization, and storage (CCUS) in recent years, shale oil, as a fossil fuel, also has a clean future [2]. The exploration and development of shale oil remains an effective way to address the problem of the huge demand for fossil fuels, despite that hydrogen energy and gas hydrate are also potential energy sources [3–5]. Shale oil exploration and development, such as those conducted in the Qingshankou Formation in Songliao Basin, Shahejie Formation in Bohai Bay Basin, Luchaogou Formation in Jimusaer Sag, and Funing Formation in Subei Basin, have made breakthroughs in China [6–11]. However, many challenges are yet to be overcome, and most of these

challenges are associated with the movability of shale oil present in the thick lacustrine shales in China [12]. Shale oil movability is closely related to the oil occurrence states in the shale pore networks [13]. Shale oil is generally adsorbed on shale pore surfaces and organic matter (adsorbed oil) and in its free form in large shale pores or fractures, with some of the shale oil dissolved in water [14–17]. Moreover, both the movability and occurrence states of shale oil are primarily influenced by the features of shale pore networks, such as pore types, sizes, and distributions [12]. Thus, the analytical results of pore network characteristics will give an insight into the micro-occurrence characteristics of shale oil.

Various technologies and methods have been developed to observe shale pore networks. Quantitative evaluation techniques, such as gas (N_2 and CO_2) adsorption, mercury intrusion capillary pressure (MICP), and nuclear magnetic resonance (NMR), are widely used to characterize shale pore structures, including porosity, permeability, and pore size distribution (PSD) [18–22]. However, these techniques have failed to provide the required intuitive information. Imaging methods, such as scanning electron microscopy (SEM) technologies, including argon ion beam milling–SEM (AIM–SEM) [23–27], focused ion beam milling–SEM (FIB–SEM) [28,29], and broad ion beam milling–SEM (BIB–SEM) [30–33], are useful for observing shale pore networks directly. These methods provide information on the actual type, size, and morphology of the pores. FIB–SEM is an alternative tool that can be employed to display three-dimensional shale pore networks. However, this tool is strongly affected by pore heterogeneity leading to poor representativeness in small high-resolution fields of view [29]. To reduce the impact of pore heterogeneity, BIB–SEM can be used to analyze shale pore network distributions by imaging on a large 1–2 mm^2 plane [30–32]. However, AIM–SEM is the most common technology employed to characterize shale pores because it can provide information on pore type, size, morphology, and distribution.

SEM images are generally used to analyze shale pore types qualitatively. The pore types in gas shales (high–over mature shales), including organic pores, interparticle pores, intraparticle pores, and intercrystal pores, have been well identified [34–37]. Organic pores primarily contribute to the occurrence spaces of shale gas. Thus, gas shale pores can be classified into organic, interparticle, and intraparticle pores [38]. However, oil shales (shale oil reservoirs) are characterized by a large number of inorganic pores and few organic pores [39–41]. Intraparticle pores in clay mineral aggregates, interparticle pores at the edges of brittle particles, dissolution pores, and intercrystal pores in pyrite aggregates are typically observed in oil shales.

Shale pore structures can be quantitatively analyzed using SEM images combined with software such as ImageJ, Photoshop, and ArcGIS [30,33,42]. Interparticle pores associated with organic matter and clay, interparticle and intraparticle pores associated with rigid minerals, and dissolution pores are quantitatively characterized to obtain the PSDs in shales [43]. Using ImageJ software, Wang et al. [44] discussed the heterogeneity of interparticle, intraparticle, and organic pores in gas shales using fractal and multifractal methods. However, because of pore heterogeneity, shale pore distributions cannot be accurately observed using a single AIM–SEM image. Although BIB–SEM images can characterize the shale pore distributions well, they are not widely used owing to their high cost. Thus, a quantitative method is required to analyze the size, morphology, and distribution of different shale pores based on AIM–SEM images.

This study aimed to establish a method for quantitatively characterizing shale pore networks in different lithofacies. AIM–SEM was first performed on shale samples from the Shahejie Formation in Donging Sag, Bohai Bay Basin. The SEM images were quantitatively analyzed by Photoshop and ImageJ software to determine the pore size, morphology, and content in different shales. Moreover, MICP was also conducted to analyze the results obtained from SEM to provide insight into the pore structures of shale oil reservoirs.

2. Samples and Methodologies

2.1. Samples

A total of 10 shale samples were collected from the Paleogene Shahejie Formation in Dongying Sag, Bohai Bay Basin. Dongying Sag, one of the most petroliferous sags in China, is the main shale oil exploration area [21]. SEM and X-ray diffraction (XRD) were performed on the selected cores, and the total organic carbon (TOC) and MICP measurements were taken to characterize the pore types and controlling factors of the cores.

2.2. SEM Method

2.2.1. SEM Imaging

The shale cores were first washed oil at 90 °C for 72 h using the dichloromethane and acetone (3:1 in volume) solvent, and after that, the cores were dried in a vacuum at 110 °C for 24 h. After cooling the cores to room temperature (about 20 °C), argon ion beam hand polishing and milling were used to flatten the core surfaces. Backscattered electron SEM images of the shale cores were obtained using an FEI Quanta 200F field emission scanning electron microscope from FEI company in the Netherlands, with its magnifications falling in the range from ×190 to ×80,000. Energy-dispersive X-ray spectroscopy (EDX) detector was used to determine the minerals contained in the shale core samples.

2.2.2. Pore Extraction

In this study, a series of SEM images taken at a given resolution were spliced using Adobe Photoshop software CS6 to reduce the influence of pore heterogeneity on the PSD. The resolutions and grayscales of the images remained unchanged during the process. Subsequently, each pore in the merged images was manually filled with a designated color to distinguish the different pore types: red was used to indicate interparticle pores, blue to indicate intraparticle pores in the clay minerals (hereinafter referred to as intraparticle pores), cyan to indicate dissolution pores, magenta to indicate the intercrystal pores in the pyrite aggregates and yellow to indicate fracture as illustrated in Figure 1a. Each pore type was identified using the "color threshold" tool in ImageJ software and then extracted using its "analyze particles" tool to obtain the image of each pore type, as displayed in Figure 1b–d. The pore morphology parameters were also obtained, such as pore circularity, elongation, and convexity. The PSD was obtained using a continuous-PSD model [45].

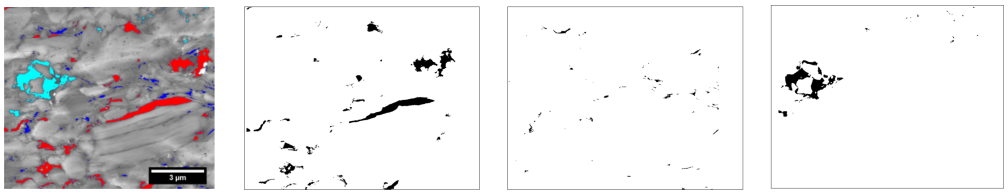

(**a**) (**b**) (**c**) (**d**)

Figure 1. Pore identification and extraction: (**a**) Pore identification; (**b**) Extraction of interparticle pores; (**c**) Extraction of clay mineral intraparticle pores; (**d**) Extraction of dissolution pores.

3. Results and Discussion

3.1. Shale TOC, Mineral Compositions, and Lithofacies

The TOC contents of the selected shale samples ranged from 0.32% to 2.68%, with an average of 1.53%, while the content of S_1 was between 0.09 and 2.96 mg/g, with an average of 0.71 mg/g (Table 1). The shale samples mainly comprised clay minerals, quartz, and calcite (Table 1). Clay minerals varied from 14% to 55.5% (mean 35.32%), followed by quartz with an average of 28.52% (17.5–40%), and calcite is between 1.8% and 31.6% (mean 14.51%). Moreover, shales also contain a small amount of feldspar (mean 8.28%), dolomite (mean 8.26%), orthoclase (mean 2.32%), and pyrite (mean 3.36%). As displayed in Figure 2, the ten studied samples included four types of lithofacies: argillaceous, felsic-rich,

felsic, and calcareous shales. Calcareous shales have the largest TOC content, followed by argillaceous shale. Both felsic-rich and felsic shales contain lower TOC contents.

Table 1. Shale TOC contents, mineral compositions, and lithofacies.

Sample	Lithofacies	TOC	S_1 mg/g	Clay Mineral/%	Quartz %	Orthoclase %	Feldspar %	Calcite %	Dolomite %	Pyrite %
S1	argillaceous	1.44	0.22	55.5	30.8	2.1	7.9	3.6		
S2	felsic-rich	1.66	0.29	14.0	38.7	5.8	18.5	11.2	6.6	0.5
S3	felsic-rich	0.32	0.09	32.1	37.7	4.8	10.5	2.3	8.3	
S4	felsic-rich	0.36	0.09	28.9	40.0	2.8	14.2	1.8	8.9	
S5	felsic	0.67	0.17	39.8	30.8	1.8	11.1	6.1	10.3	
S6	felsic	0.51	0.10	36.7	24.1	1.5	10.1	16.7	5.9	5.1
S7	calcareous	2.60	1.51	40.7	17.5	0.9	3.1	26.5	1.8	4.5
S8	calcareous	2.68	0.46	37.0	20.0	1.7	2.5	31.6		2.2
S9	calcareous	2.58	1.25	38.5	19.8	1.6	2.2	26.6	6.8	4.5
S10	calcareous	2.52	2.96	30.0	26.0	0.2	2.7	18.7	17.5	4.8

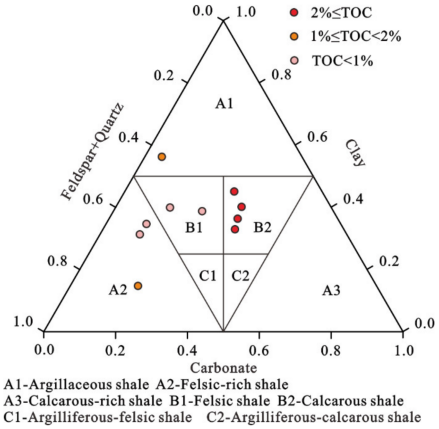

Figure 2. Lithofacies of the selected shales.

3.2. Pore Types and Distributions of Different Lithofacies

In this study, a total of 77 SEM images from 10 shales were analyzed. The image quantity of each sample is listed in Table 2, the resolutions of the SEM images fell in the range from 8.35 to 23.83 nm. The extracted pore quantity varied from 1032 to 3526, with a mean of 2288, while fracture quantity was between 6 and 78, with an average of 33.

Table 2. Number and resolution of SEM images, pores, and fractures.

Sample	Lithofacies	SEM Images Number	Resolution/nm	Pore Number	Fracture Number
S1	argillaceous	9	10.4	2255	23
S2	felsic-rich	6	23.83	3526	76
S3	felsic-rich	4	12.84	1368	7
S4	felsic-rich	4	23.83	2119	78
S5	felsic	9	10.4	1975	64
S6	felsic	9	10.4	3373	16
S7	calcareous	9	10.4	1599	6
S8	calcareous	9	10.4	1032	6
S9	calcareous	9	8.35	2937	14
S10	calcareous	9	10.4	2694	40

3.2.1. Argillaceous Shale

Among the different types of shales, argillaceous shale (S1) has the largest clay mineral content (Table 1), resulting in plenty of intraparticle pores, as displayed in Figure 3. The

intraparticle pores with a complex morphology varying from plate-like to irregular serrated shapes occur in clay mineral aggregates. The interparticle pores at the edges of quartz particles are another major type of pores with complex irregular shapes. Meanwhile, a few dissolution pores also were identified. The morphological parameters of interparticle, intraparticle, and dissolution pores are displayed in Figure 4a–c. The pore circularity distributions indicate that the dissolution pores in argillaceous shale have the largest circularity with almost circular shapes, followed by intraparticle and interparticle pores (Figure 4a). By contrast, dissolution pores have the smallest elongations (Figure 4b). Moreover, the interparticle pores have the roughest edges and the largest convexity, whereas the dissolution pores have opposite characteristics, as shown in the SEM images in Figure 3.

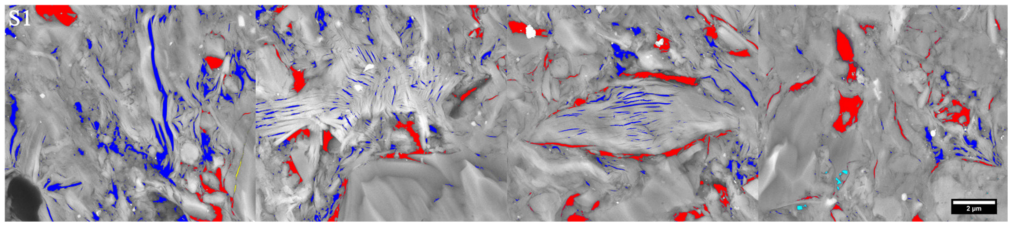

Figure 3. Pore identification in argillaceous shale. Red represents interparticle pores, blue represents intraparticle pores, cyan represents dissolution pores.

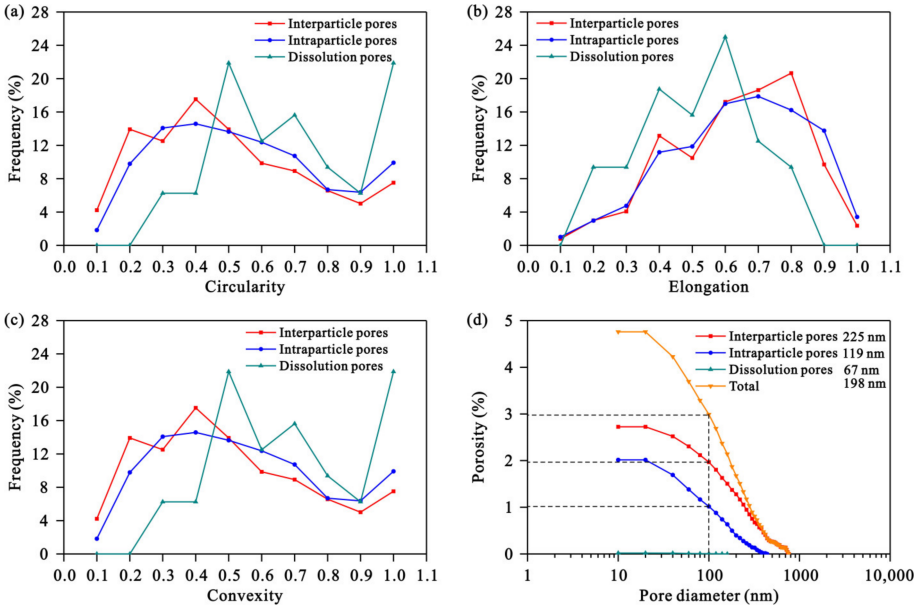

Figure 4. Pore morphology parameters and pore size distributions in argillaceous shales: (**a**) Circularity; (**b**) Elongation; (**c**) Convexity; (**d**) Pore size distributions.

Figure 4d displays the PSDs of different types of shales: argillaceous shale consists of numerous mesopores (0.1–1 μm), moderate micropores (<1 μm), and an average pore diameter of 198 nm. Furthermore, interparticle pores are larger than intraparticle pores, and their average pore diameters are 225 nm and 119 nm, respectively. The dissolution pores have the smallest pore size, characterized by an average pore diameter of 67 nm.

3.2.2. Felsic-Rich Shale

Felsic-rich shales have large quantities of felsic minerals, including quartz, feldspar, and orthoclase; the felsic mineral granules form rock skeletons with clay minerals filling the intergranular shale pores (Figure 5). Consequently, intraparticle pores are developed in clay minerals, while at the edges of felsic mineral granules interparticle pores are

developed. Moreover, dissolution pores occur in orthoclase and feldspar granules, as shown in Figure 5a,b. However, the dissolution pores are not developed in sample S4 (Figure 5c). The circularity of the dissolution pores with a shape similar to a circle is the largest, followed by the circularities of intraparticle and interparticle pores. Pore elongation is different from the behavior of argillaceous shales (Figure 6a,b). Furthermore, the dissolution pores have the smoothest morphology, followed by the morphologies of intraparticle and interparticle pores in that order (Figure 6c).

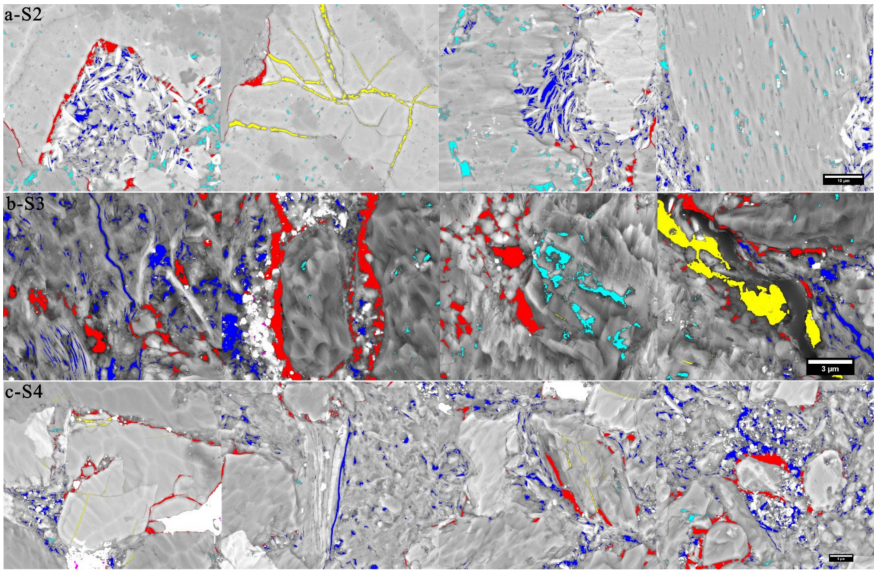

Figure 5. Pore identifications in felsic-rich shales: (**a**) S2; (**b**) S3; (**c**) S4. Red represents interparticle pores, blue represents intraparticle pores, cyan represents dissolution pores and yellow represents fracture.

Felsic-rich shales have higher contents of intraparticle and dissolution pores than argillaceous shales (Figure 6d–f). Sample S2 has the largest pore size with an average pore diameter of 381 nm and is characterized by a large number of mesopores, a moderate number of micropores, and a small number of macropores (>1 μm). Intraparticle pores make the most considerable contribution to the pore volume of S2. By contrast, interparticle pores have the largest pore size with an average diameter of 481 nm (Figure 6d). Similarly, the intraparticle pore content of S4 is larger than its interparticle pore content (Figure 6e). The average pore diameters of the total pore system and interparticle, intraparticle, and dissolution pores are 364, 474, 251, and 297 nm, respectively (Figure 6e). However, S3 has a larger number of interparticle pores than intraparticle pores. The average pore diameters of interparticle, dissolution, and intraparticle pores decrease in that order (Figure 6f). Moreover, it is found that in felsic-rich shales, interparticle pores are the largest in size, followed by dissolution and intraparticle pores (Figure 6e,f).

The pore types of felsic-rich shales are influenced by their mineral compositions. As listed in Table 1, the clay mineral contents of S2, S4, and S3 increase in that order, while their felsic and calcareous mineral contents decrease in the same order. The average pore diameters of the total pore system and interparticle, intraparticle, and dissolution pores decrease with increasing clay mineral content, as illustrated in Figure 7a. The interparticle pores are more developed, while intraparticle pores are on the contrary (Figure 7b). It can be explained that interparticle pores generally occur between the felsic granule and clay minerals. Thus, higher clay mineral contents result in more pores at the edge of the felsic granules. However, shales being plastic minerals, their plasticity increases as their clay mineral contents increase, corresponding to a decrease in their compaction resistance, resulting in pore size reduction [37]. Therefore, the pore structures of felsic-rich shales are mainly controlled by their clay mineral contents, and a higher content of clay minerals leads to a larger number of interparticle pores with smaller pore sizes.

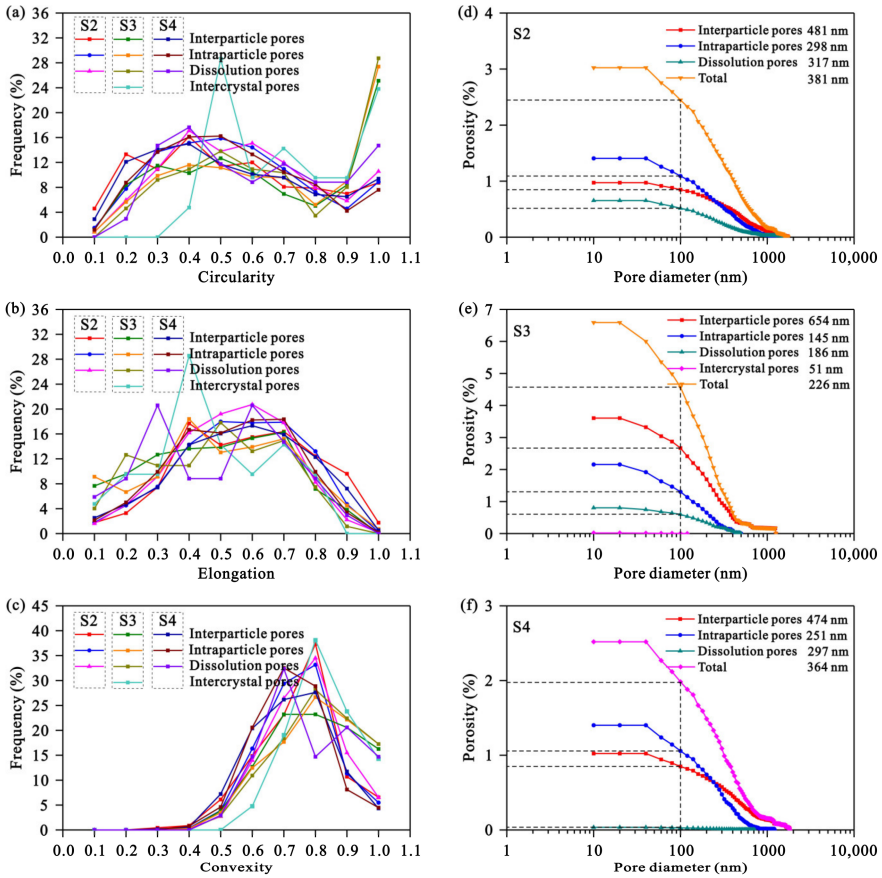

Figure 6. Pore morphology parameters and pore size distributions in felsic-rich shales: (**a**) Circularity; (**b**) Elongation; (**c**) Convexity; (**d**) Pore size distribution of S2; (**e**) Pore size distribution of S3; (**f**) Pore size distribution of S4.

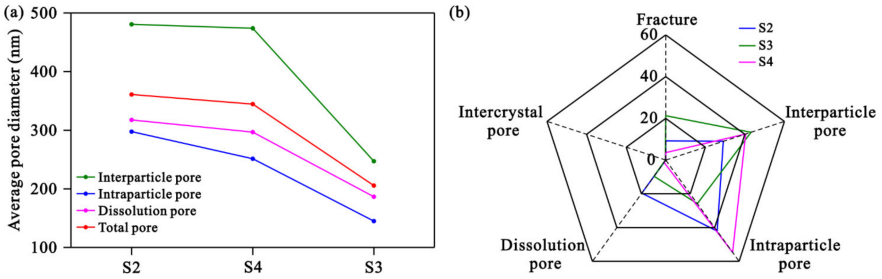

Figure 7. Pore size and type distributions in felsic-rich shales: (**a**) Average pore diameter; (**b**) Pore type distributions.

3.2.3. Felsic Shales

Felsic shales have a lower content of felsic minerals and a higher content of clay minerals than felsic-rich shales. Therefore, felsic shales have more interparticle pores than intraparticle pores, as shown in Figure 8. Moreover, dissolution pores would develop in a felsic shale, such as in sample S6, if the shale has a high content of calcareous minerals, as displayed in Figure 8b. The morphologies of the different pore types show that argillaceous and felsic-rich shales have similar pore distributions. Interparticle pores have the most complex shapes, whereas dissolution pores have the simplest shapes (Figure 9). S5 has a large average pore diameter of 309 nm with the largest number of dissolution pores (mean 421 nm in diameter) and the smallest number of intraparticle pores (mean 163 nm) (Figure 10a). However, the interparticle pores of S6 have the largest pore sizes (mean 338 nm), followed by intraparticle

(131 nm) and dissolution pores (100 nm) (Figure 10b). Although the intercrystal pores in felsic shales are large, they are poorly developed.

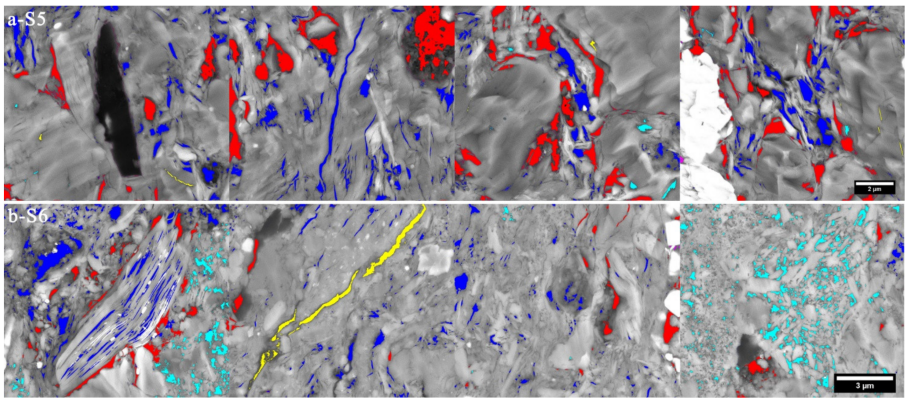

Figure 8. Pore identification in felsic shales: (**a**) S5; (**b**) S6. Red represents interparticle pores, blue represents intraparticle pores, cyan represents dissolution pores and yellow represents fracture.

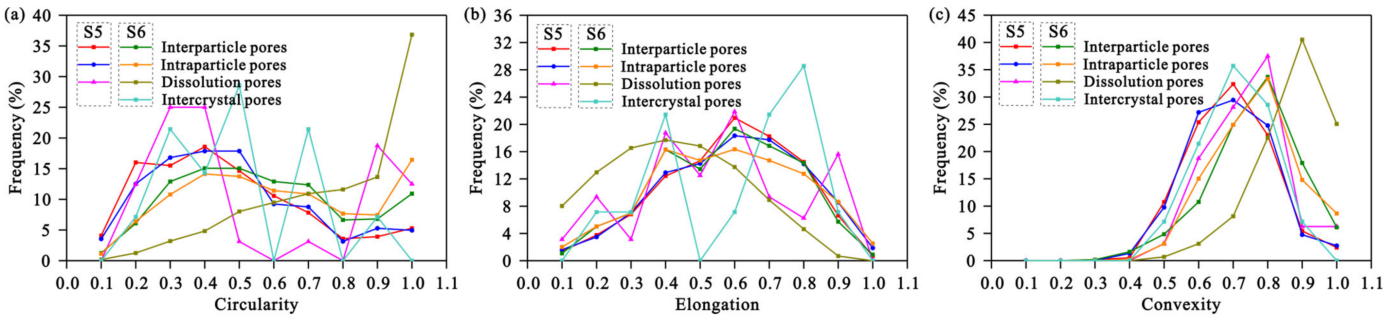

Figure 9. Pore morphology parameters in felsic shales: (**a**) Circularity; (**b**) Elongation; (**c**) Convexity.

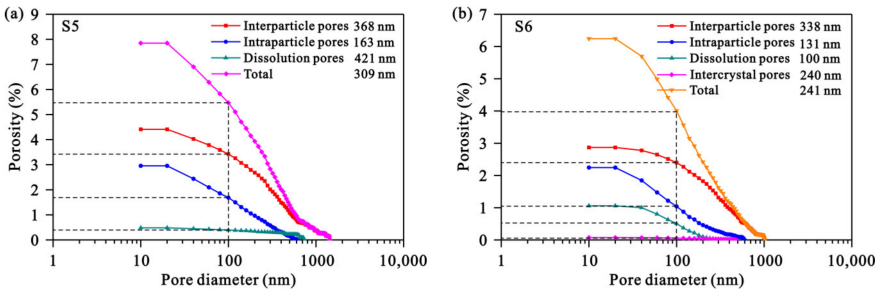

Figure 10. Pore size distributions in felsic shales: (**a**) S5; (**b**) S6.

The clay and felsic mineral contents of S6 are less than those of S5, whereas the calcareous mineral content of S6 is higher than that of S5 (Table 1). Both quartz and feldspar are brittle minerals; thus, as the felsic mineral content decreases, the anticompaction ability of the minerals will also decrease, resulting in a decreased pore size (Figure 11a). The interparticle pores do not fully develop when the clay and felsic mineral contents are low, as displayed in Figure 11b. However, if the calcareous mineral content is large, as in S6, the dissolution pores may develop because calcareous minerals easily dissolve in organic acid generated during the hydrocarbon generation process [46]. Therefore, felsic minerals primarily control the felsic shale reservoir properties, while calcareous minerals control dissolution pore development.

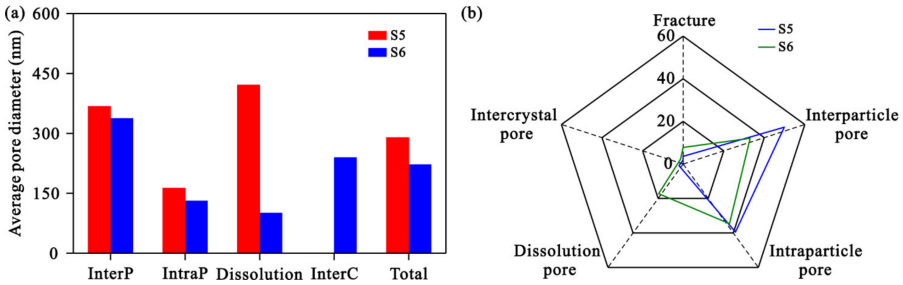

Figure 11. Pore size and type distributions in felsic shales: (**a**) Average pore diameter; (**b**) Pore type distributions.

3.2.4. Calcareous Shales

Calcareous shales mainly comprise clay and calcareous minerals, characterized by large TOC contents (Table 1 and Figure 2). The high clay mineral contents result in the development of intraparticle pores (Figure 12). The interparticle pores include pores between or at the edges of granules, as illustrated in Figure 12a. Because of the high calcite content, the dissolution pores could develop, as displayed in Figure 12c. Moreover, intercrystal pores can be present in strawberry pyrite aggregates (Figure 12d). Thus, calcareous shales mainly develop intraparticle and interparticle pores, while as in S9 and S10, they may develop many dissolution and intercrystal pores if the dissolution and pyrite develop. The dissolution and intercrystal pores are round and polygonal, respectively, corresponding to high circularity values, indicating almost circular shapes (Figure 13a,b). The interparticle pores generally occur at the edges of granules of irregular shapes, leading to low circularity values (Figure 13a,b). Pore elongation behaves oppositely (Figure 13c,d). The dissolution and intercrystal pores commonly have smooth pore edges characterized by high convexities (Figure 13e,f).

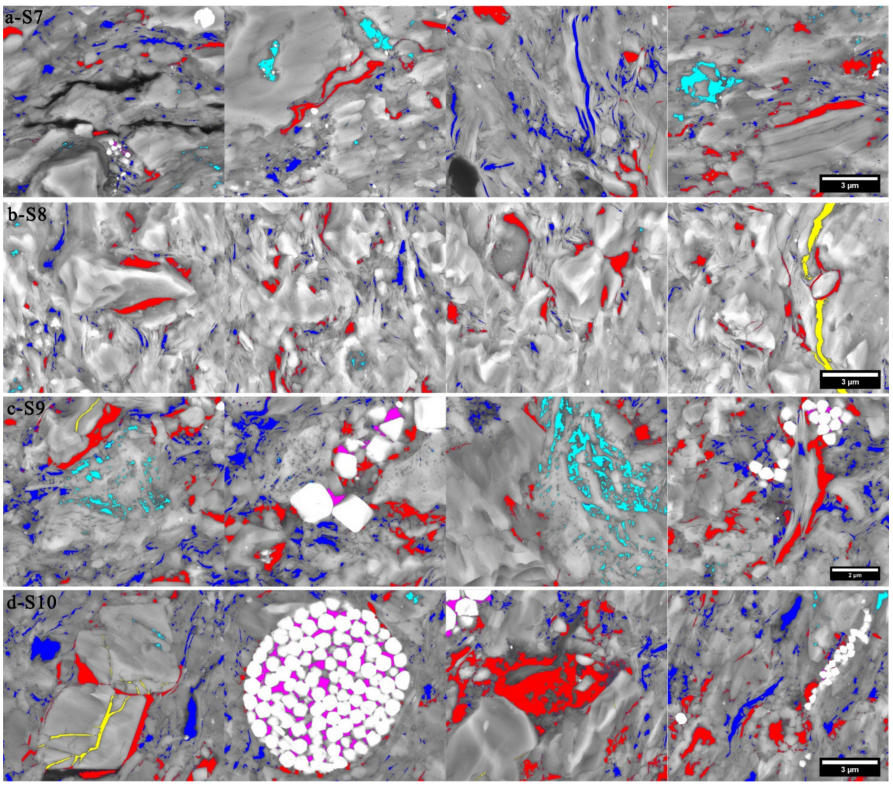

Figure 12. Pore identification in calcareous shales: (**a**) S7; (**b**) S8; (**c**) S9; (**d**) S10. Red represents interparticle pores, blue represents intraparticle pores, cyan represents dissolution pores, magenta represents intercrystal pores in the pyrite aggregates and yellow represents fracture.

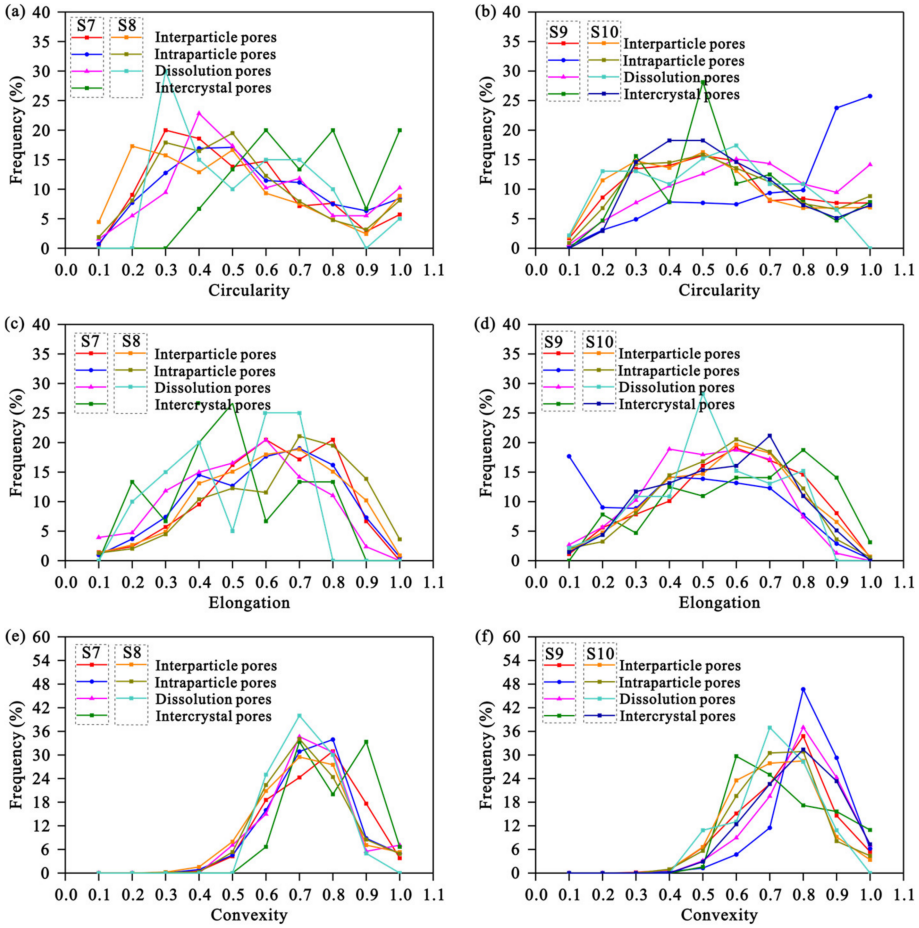

Figure 13. Pore morphology parameters in calcareous shales: (**a**) Circularity distribution of S7 and S8; (**b**) Circularity distribution of S9 and S10; (**c**) Elongation distribution of S7 and S8; (**d**) Elongation distribution of S9 and S10; (**e**) Convexity distribution of S7 and S8; (**f**) Convexity distribution of S9 and S10.

The average pore diameters of the calcareous shales in the four samples range from 204 to 232 nm (mean 221 nm), indicating that calcareous shales contain developed micropores (Figure 14). The dissolution pores in S7 are the largest with an average diameter of 245 nm, followed by interparticle pores (mean 136 nm), intraparticle pores (mean 110 nm), while the intercrystal pores are the smallest (mean 78 nm) (Figure 14a). S9 has a large pore size with large interparticle pores (an average diameter of 342 nm) and contains numerous mesopores, a moderate number of micropores, and few macropores (Figure 14c). The interparticle pores in S8 and S10 are the largest, while their dissolution pores are the smallest (Figure 14b,d). S10 has a small number of large intercrystal pores with an average diameter of 157 nm. Moreover, both S7 and S9 have high contents of S1 (Table 1), implying that a high content of organic acid has been generated, causing dissolution pores to develop (Figure 14a,c). However, although S10 has the largest S1 content, it has only a few dissolution pores. The low number of dissolution pores in S10 could be attributed to its high dolomite content, which is much larger than that in each of the other samples (Table 1). Previous studies indicate that calcite may corrode more easily than dolomite does [46].

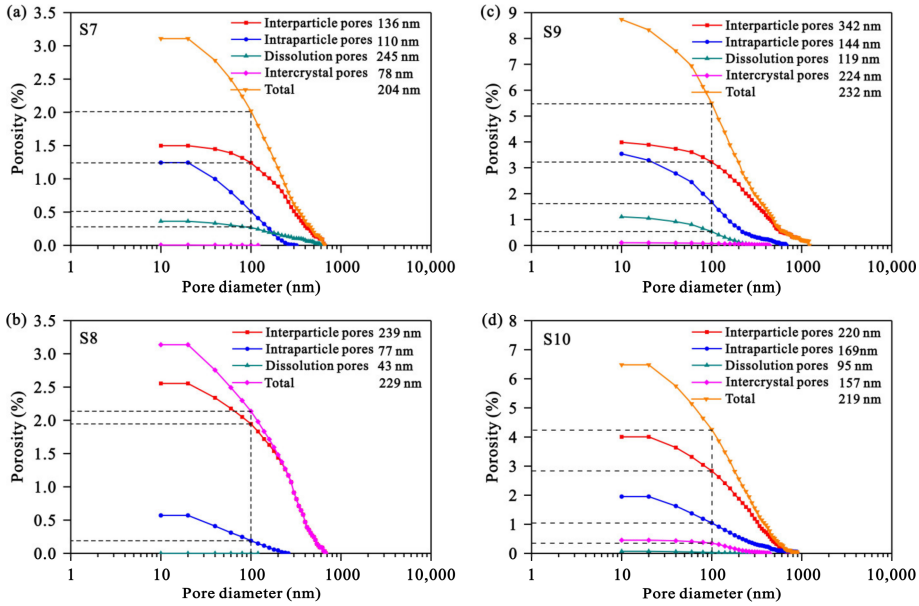

Figure 14. Pore size distributions in calcareous shales: (**a**) S7; (**b**) S7; (**c**) S9; (**b**) S10.

As the clay mineral contents of the samples increase (in the order of S10, S8, and S9 to S7), the average pore diameters of the total pore system and intraparticle pores tend to decrease. In contrast, the average diameters of the dissolution pores tend to increase (Figure 15a). The average pore diameter of the total pore system decreases from 319 to 204 nm (Figure 14). The average diameters of the dissolution pores in S7 and S9 increase from 95 to 245 nm (Figure 14) owing to the large number of dissolution pores present in the two samples. Moreover, the average pore diameters of the dissolution pores decrease as the calcareous mineral content increases because when the calcareous mineral content is low, an increased number of calcite particles are dissolved, resulting in large dissolution pores. Moreover, shale pore types are related to shale mineral compositions. As the clay mineral content of a shale increases, its plasticity also increases, lowering the fractures in the shale; felsic minerals behave oppositely (Figure 15b). Similar phenomena occur in interparticle pores as well. Therefore, the pore types of calcareous shale are primarily controlled by the clay and felsic minerals, while calcite is critical to dissolution pore development. Higher content of dissolution pores typically corresponds to a larger shale oil content.

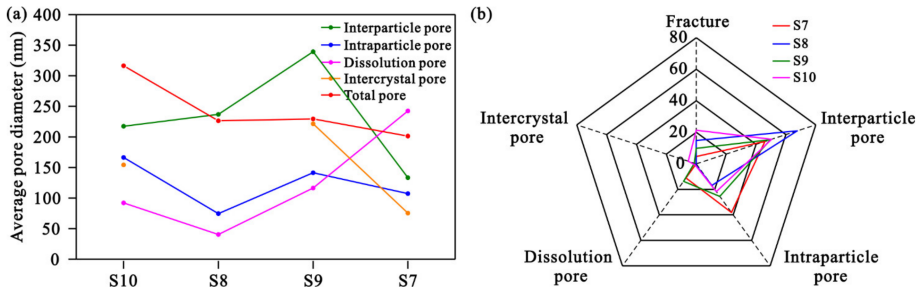

Figure 15. Pore size and type distributions in calcareous shales: (**a**) Average pore diameter; (**b**) Pore type distributions.

3.3. Comparison of Different Lithofacies

The porosity of each pore type in the four lithofacies shales considered in the study is listed in Table 3 and displayed in Figure 16. The porosity of interparticle pores ranges from 0.973% to 4.521% (mean 2.570%), characterized by the largest values for calcareous shales (mean 3.071%), followed by argillaceous shale (mean 2.724%), felsic shales (mean 2.540%),

and felsic-rich shales (mean 1.872%) (Figure 16a). The intraparticle pore porosity, which falls within the range of 0.570–2.752%, has an average of 1.755%; it is highest in felsic shales and lowest in calcareous shales (Figure 16a). The dissolution pore porosity varying from 0.019% to 1.104% with an average of 0.437%, is primarily controlled by the content and dissolution of calcite, contained in S6, S7, and S9. However, generally, the intercrystal pores in pyrite aggregates with an average pore porosity of 0.114% (0.004–0.485%) are not the main pore space in shales, Pyrite aggregates are commonly associated with organic matter, corresponding to organic-rich shales, such as calcareous shales considered in this study, which have developed intercrystal pores (Figure 16b).

Table 3. Porosity and average diameters of different types of pores in the studied shales.

Sample	Porosity/%						D_a*/nm
	Fracture	Interparticle Pore	Intraparticle Pore	Dissolution Pore	Intercrystal Pore	Total Pore	
S1	0.120	2.724	2.015	0.019		4.758	198
S2	0.310	0.973	1.407	0.654		3.034	381
S3	1.778	3.606	2.157	0.804	0.018	6.585	226
S4	0.092	1.037	1.402	0.035		2.473	364
S5	0.114	3.287	2.752	0.216	0.004	6.259	309
S6	0.319	1.794	2.005	1.059	0.070	4.928	241
S7	0.153	1.498	1.244	0.363	0.004	3.108	204
S8	0.498	2.278	0.570	0.022		2.870	229
S9	0.789	3.986	2.050	1.104	0.104	7.244	232
S10	1.910	4.521	1.951	0.091	0.485	7.048	219

* Da is the average pore diameter.

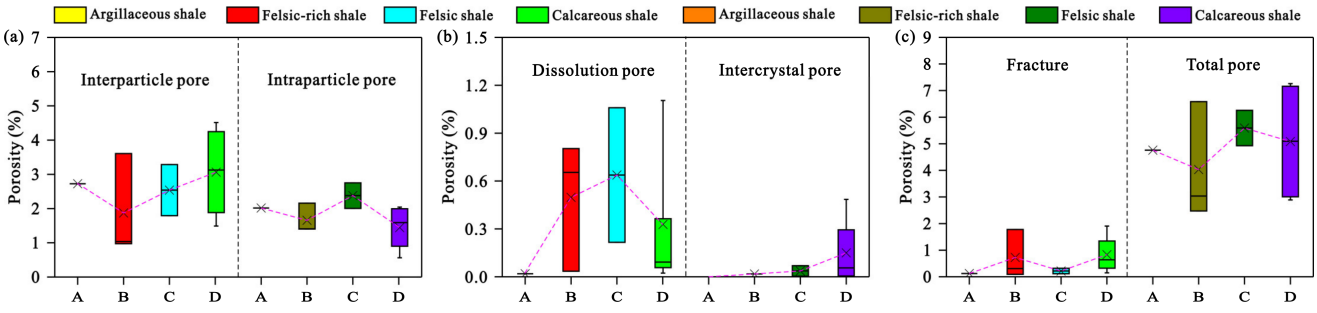

Figure 16. Porosity distributions of different pore types in the four lithofacies shales: (**a**) Interparticle pore and intraparticle pore; (**b**) Dissolution pore and intercrystal pore; (**c**) Fracture and total pore.

The total porosity of the four types of pores considered ranges from 2.473% to 7.244% with an average of 4.831%, and the felsic shales have the largest porosity, followed by calcareous shales, as shown in Figure 16c. Moreover, fractures are important seepage channels that play a key role in shale oil development. The fracture porosity is between 0.092% and 1.910%, with a mean of 0.608%. Felsic-rich and calcareous shales contain numerous fractures because of their large brittle mineral contents (Figure 16c). Thus, interparticle and intraparticle pores primarily contribute to the pore space in shale oil reservoirs, while dissolution pores would play an essential role if the calcite in the shales, especially in calcareous shales, is corroded (Figure 12a,c). Therefore, dissolution pores are mainly responsible for improving the physical properties of shale oil reservoirs in the oil window, and a larger number of dissolution pores implies a larger content of shale oil (Table 1 and Figure 12). The pore sizes imply that a larger content of clay minerals generally corresponds to a smaller pore size, while the opposite is true with felsic minerals. Thus, felsic-rich shales have the largest pore sizes, while argillaceous shales have the smallest pore sizes, as exhibited in Figure 17.

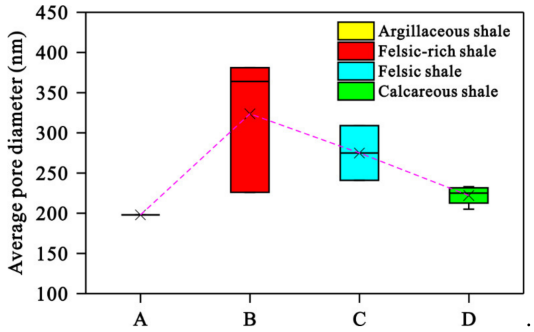

Figure 17. Average pore diameters of the four lithofacies shales.

Previous studies have paid attention to the classification of gas shale pores. High/over maturity in gas shales indicates that the shales have undergone high compaction, resulting in poorly developed inorganic pores, especially interparticle pores. In contrast, pores formed in organic matter primarily contribute to the pore space in gas shales [34,38]. Because of high compaction, most pores in gas shales are less than 100 nm in diameter, and the pore diameters of organic pores are mostly between 40 and 60 nm [43,44]. Therefore, the gas shale pores can be primarily classified into three types: organic, interparticle, and intraparticle pores [38]. The pore networks of gas shales can be further divided into organic, interparticle, intraparticle, and mixed pore networks. However, compared with high/over-maturity gas shales, the lacustrine shales (oil shales) of low maturity have undergone low compaction and simultaneous low-temperature heating. The inorganic pores, especially the interparticle pores, can be largely preserved in oil shales. Interparticle pores commonly occur between clay minerals and brittle materials, such as quartz, while intraparticle pores are mainly developed in clay mineral aggregates or as dissolution pores in granules [40]. However, because of their low maturity, organic pores fail to develop [6]. Therefore, oil shales mainly develop inorganic pores, including interparticle and intraparticle pores, with their sizes ranging from several nanometers to values exceeding 1 μm [47]. Complex compositions and large molecular diameters cause shale oil to have poor flow capacity [13]. Fractures play a crucial role in shale oil seepage. Thus, this study considered fractures, interparticle pores, and intraparticle pores as the three elements when dividing shale oil reservoir pore networks, as displayed in Figure 18. Note that the intraparticle pores in the figure include the intraparticle pores in the clay mineral aggregates and dissolution pores. The argillaceous shale has an interparticle pore network because of the presence of developed interparticle pores at the edges of quartz granules (Figure 3). The felsic-rich shales mainly contain intraparticle pore networks, with pores mainly occurring in the clay minerals present in between particles (Figure 5). The pore networks of felsic shales vary depending on the extent to which dissolution pores have been developed (Figure 8). Mixed-pore networks primarily characterize the calcareous shales because of fracture development (Figure 12).

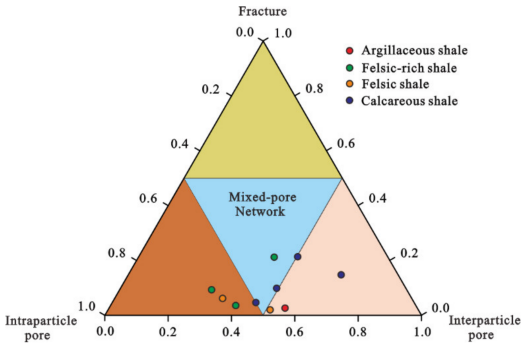

Figure 18. Pore type distributions of the four lithofacies shales.

3.4. Comparison between SEM and MICP

The PSDs of four lithofacies shales obtained from SEM and MICP are illustrated in Figure 19. The PSDs determined by SEM indicate that lacustrine shale pores mainly consist of mesopores, micropores, and a few macropores. The pore sizes obtained from SEM generally range from 20 nm to 2 μm and are much larger than gas shale pores [43,44]. However, previous studies revealed that lacustrine shale pores less than 20 nm and higher than 2 μm in diameter could be detected using nitrogen adsorption and NMR 45. This phenomenon can be explained as follows: owing to the limitation of SEM image resolutions (Table 2), identifying pores less than 20 nm in diameter is difficult; the large macropores also cannot be observed because of the small imaging area [30]. Thus, SEM is an effective and intuitive technology that can analyze pores, especially mesopores, ranging from dozens of nanometers to microns in diameter [42].

A discrepancy exists between the PSDs obtained using SEM and MICP, as illustrated in Figure 19. MICP PSDs display that pore throat diameters in lacustrine shales are less than 100 nm and that most pore throat diameters are less than 20 nm, which is much lower than the values obtained using SEM. Thus, MICP primarily detects the shale pore throat size rather than the shale pore body size because of the "pore shielding effect" [48,49]. MICP underestimates the pore volume related to large pores and simultaneously overestimates the intrusion volume of micropores, especially those less than 20 nm in diameter. As a result, MICP mainly detects the throats and the pore volumes connected by tiny throats. Thus, pores in shale oil reservoirs have various sizes but are connected by tiny throats, most of which are less than 20 nm in diameter. For example, in calcareous shales, the pore sizes range from 20 nm to 2 μm with an average of 221 nm, and most of the throats are less than 20 nm in diameter. Shale oil, which occurs in pores of several sizes, has to flow through tiny throats, which is the main factor leading to the poor fluidity of shale oil.

As discussed, lacustrine shales primarily develop interparticle pores at the edges of brittle particles and intraparticle pores in clay mineral aggregates. The pore size in these shales is mainly controlled by their clay and felsic mineral contents, and an increase in the clay mineral content will decrease the pore size. The interparticle pores are generally characterized by pore sizes larger than the sizes of intraparticle pores. Moreover, dissolution pores are crucial for improving shale reservoir properties, and they provide more space for shale oil. Among the four studied lithofacies shales in the Dongying Sag, felsic-rich shales generally have the largest pore sizes and throats, which is conducive to the accumulation and flow of shale oil. However, the TOC contents of felsic-rich shales are low; thus, these shales can produce little oil by themselves. Therefore, the felsic-rich shales can form intercalated shale oil only when adjacent to organic-rich shales. Moreover, calcareous shales with many dissolution pores and large TOC contents can produce matrix-type shale oil characterized by self-generation and self-storage. Thus, it can be concluded that organic-rich calcareous shales with lamina, which leads to the development of fractures, are favorable for shale reservoirs. However, argillaceous and felsic shales, especially felsic shales with few fractures and tiny throats, may not be favorable for shale oil reservoirs.

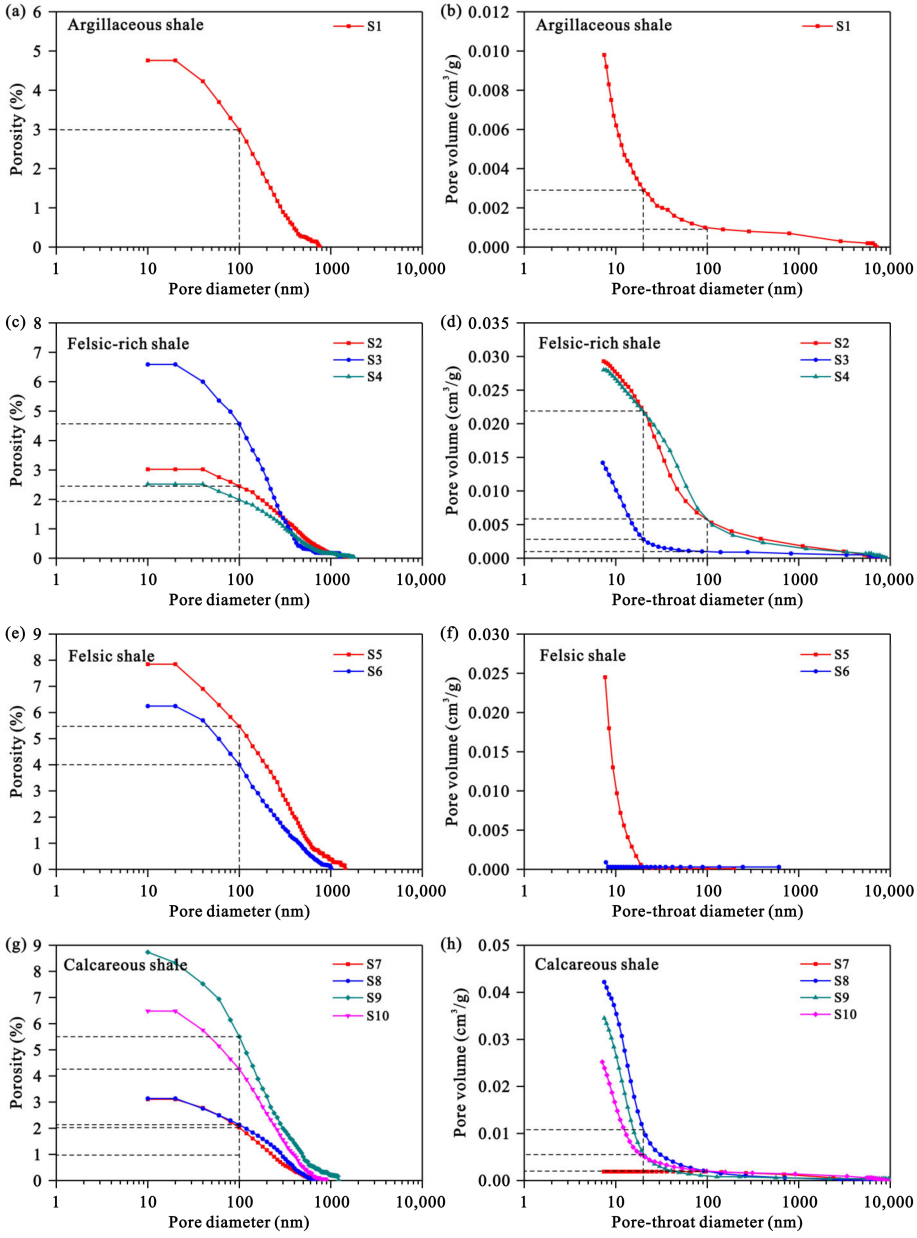

Figure 19. Pore/throat size distribution in shales: (**a**) Pore size distribution of argillaceous shales; (**b**) Pore throat distribution of argillaceous shales; (**c**) Pore size distribution of felsic-rich shales; (**d**) Pore throat distribution of felsic-rich shales; (**e**) Pore size distribution of felsic shales; (**f**) Pore throat distribution of felsic shales; (**g**) Pore size distribution of calcareous shales; (**h**) Pore throat distribution of calcareous shales.

4. Conclusions

Using the SEM images, this study quantitatively examined the pore distributions of four lithofacies lacustrine shales obtained from the Dongying Sag, Bohai Bay Basin, China. The pore types, morphologies, and sizes of the four studied lithofacies shales, and their contents were analyzed. Four types of pores and fractures, including interparticle pores at the edges of brittle particles, intraparticle pores in clay mineral aggregates, dissolution pores, and intercrystal pores in pyrite aggregates, were identified in oil shales. Interparticle and intraparticle pores primarily contribute to the shale oil spaces. Moreover, dissolution pores may be developed in calcite-rich shales because of their dissolution owing to organic acid, and a large number of dissolution pores present would be a critical factor responsible

for making calcareous shales become a favorable shale oil reservoir. Interparticle pores commonly have complex morphologies, whereas dissolution pores have simple shapes.

The pore sizes in lacustrine shales are primarily controlled by clay and felsic minerals. Large clay mineral content in lacustrine shales generally corresponds to a small shale pore size, while felsic minerals act oppositely. SEM images indicate that the pore diameters range from 20 nm to 2 μm, while pore throat diameters are mostly less than 20 nm. Thus, lacustrine shales are commonly characterized by large pores but tiny throats, leading to poor shale oil moveability.

Felsic-rich shales are generally characterized by large pore sizes and throats, which are favorable for shale oil accumulation and seepage. Felsic-rich shales can form intercalated shale oil if adjacent to organic-rich shales. Calcareous shales with numerous dissolution pores and a large content of TOC may produce self-generation and self-storage matrix shale oil and develop fractures, producing an excellent seepage channel for shale oil.

Author Contributions: Conceptualization, J.W. and S.L.; methodology, J.W. and P.Z.; software, J.W. and P.Z.; validation, J.W. and S.L.; formal analysis, J.W.; investigation, J.W. and Q.Z.; resources, Q.Z. and H.H.; data curation, H.H.; writing—original draft preparation, J.W.; writing—review and editing, J.W.; visualization, J.W.; supervision, P.Z.; project administration, P.Z.; funding acquisition, P.Z. All authors have read and agreed to the published version of the manuscript.

Funding: This research was funded by the Natural Science Foundation of Shandong Province (ZR2020QD036). And The APC was funded by S.L.

Data Availability Statement: Not applicable.

Acknowledgments: This work was financially supported by the Natural Science Foundation of Shandong Province (ZR2020QD036).

Conflicts of Interest: The authors declare no conflict of interest.

References

1. Jarvie, D.M. Shale resource systems for oil and gas; Part 2, Shale-oil resource systems. *AAPG Mem.* **2012**, *97*, 89–119.
2. Sun, J.; Chen, X.; Wang, X.; Zhang, Y.; Qin, Y.; Chen, C.; Li, W.; Zhou, W. Displacement characteristics of CO2 to CH4 in heterogeneous surface slit pores. *Energy Fuels* **2023**, *37*, 2926–2944. [CrossRef]
3. Hu, W.; Chen, C.; Sun, J.; Zhang, N.; Zhao, J.; Liu, Y.; Ling, Z.; Li, W.; Liu, W.; Song, Y. Three-body aggregation of guest molecules as a key step in methane hydrate nucleation and growth. *Commun. Chem.* **2022**, *5*, 33. [CrossRef]
4. Chen, Z.; Liu, W.; Sun, J.; Chen, C.; Song, Y. Alanine rich amphiphilic peptides as green substitutes for hydrate inhibitors: A molecular simulation study. *J. Mol. Liq.* **2023**, *370*, 121008. [CrossRef]
5. Chen, Z.; Sun, J.; Wu, P.; Liu, W.; Chen, C.; Lang, C.; Dai, S.; Zhou, W. Cyclodextrin as a green anti-agglomerant agent in oil–water emulsion containing asphalt. *Fuel* **2023**, *335*, 127041. [CrossRef]
6. Liu, B.; Sun, J.; Zhang, Y.; He, J.; Fu, X.; Yang, L.; Xing, J.; Zhao, X. Reservoir space and enrichment model of shale oil in the first member of Cretaceous Qingshankou Formation in the Changling Sag, southern Songliao Basin, NE China. *Pet. Explor. Dev.* **2018**, *48*, 608–624. [CrossRef]
7. Xu, L.; Chang, Q.; Yang, C.; Tao, Q.; Wang, S.; Fei, J.; Xu, S. Characteristics and oil-bearing capability of shale oil reservoirs in the Permian Lucaogou Formation, Jimusaer sag. *Oil Gas Geol.* **2019**, *40*, 535–549.
8. Zhao, W.; Zhu, R.; Hu, S.; Hou, L.; Wu, S. Accumulation contribution differences between lacustrine organic-rich shales and mudstones and their significance in shale oil evaluation. *Pet. Explor. Dev.* **2020**, *47*, 1079–1089. [CrossRef]
9. Zou, C.; Pan, S.; Jing, Z.; Gao, J.; Yang, Z.; Wu, S.; Zhao, Q. Shale oil and gas revolution and its impact. *Acta Pet. Sin.* **2020**, *41*, 1–12.
10. Jin, Z.; Liang, X.; Bai, Z. Exploration breakthrough and its significance of Gulong lacustrine shale oil in the Songliao Basin, Northeastern China. *Energ. Geosci.* **2022**, *3*, 120–125. [CrossRef]
11. Zhang, P.; Lu, S.; Lin, Z.; Duan, H.; Chang, X.; Qiu, Y.; Fu, Q.; Zhi, Q.; Wang, J.; Huang, H. Key Oil Content Parameter Correction of Shale Oil Resources: A Case Study of the Paleogene Funing Formation, Subei Basin, China. *Energy Fuels* **2022**, *36*, 5316–5326. [CrossRef]
12. Lu, S.; Xue, H.; Wang, M.; Xiao, D.; Huang, W.; Li, J.; Xie, L.; Tian, S.; Wang, S.; Li, J.; et al. Several key issues and research trends in evaluation of shale oil. *Acta Pet. Sin.* **2016**, *37*, 1309–1322.
13. Li, J.; Lu, S.; Cai, J.; Zhang, P.; Xue, H.; Zhao, X. Adsorbed and Free Oil in Lacustrine Nanoporous Shale: A Theoretical Model and a Case Study. *Energy Fuels* **2018**, *32*, 12247–12258. [CrossRef]
14. Li, Z.; Zou, Y.; Xu, X.; Sun, J.; Li, M.; Peng, P. Adsorption of mudstone source rock for shale oil–Experiments, model and a case study. *Org. Geochem.* **2016**, *92*, 55–62. [CrossRef]

15. Li, J.; Lu, S.; Xie, L.; Zhang, J.; Xue, H.; Zhang, P.; Tian, S. Modeling of hydrocarbon adsorption on continental oil shale: A case study on n -alkane. *Fuel* **2017**, *206*, 603–613. [CrossRef]
16. Wang, M.; Ma, R.; Li, J.; Lu, S.; Li, C.; Guo, Z.; Li, Z. Occurrence mechanism of lacustrine shale oil in the Paleogene Shahejie Formation of Jiyang Depression, Bohai Bay Basin, China. *Pet. Explor. Dev.* **2019**, *46*, 789–802. [CrossRef]
17. Zhang, P.; Lu, S.; Li, J.; Chang, X. 1D and 2D Nuclear magnetic resonance (NMR) relaxation behaviors of protons in clay, kerogen and oil-bearing shale rocks. *Mar. Pet. Geol.* **2020**, *114*, 104210. [CrossRef]
18. Zargari, S.; Canter, K.; Prasad, M. Porosity evolution in oil-prone source rocks. *Fuel* **2015**, *153*, 110–117. [CrossRef]
19. Hu, J.; Tang, S.; Zhang, S. Investigation of pore structure and fractal characteristics of the Lower Silurian Longmaxi shales in western Hunan and Hubei Provinces in China. *J. Nat. Gas Sci. Eng.* **2016**, *28*, 522–535. [CrossRef]
20. Hu, Q.; Zhang, X.; Meng, X.; Li, Z.; Xie, Z.; Li, M. Characterization of micro-nano pore networks in shale oil reservoirs of Paleogene Shahejie Formation in Dongying Sag of Bohai Bay Basin, East China. *Pet. Explor. Dev.* **2017**, *44*, 681–690. [CrossRef]
21. Zhang, P.; Lu, S.; Li, J.; Chen, C.; Xue, H.; Zhang, J. Petrophysical characterization of oil-bearing shales by low-field nuclear magnetic resonance (NMR). *Mar. Pet. Geol.* **2018**, *89*, 775–785. [CrossRef]
22. Zhao, R.; Xue, H.; Lu, S.; Li, J.; Tian, S.; Wang, M.; Dong, Z. Multi-scale pore structure characterization of lacustrine shale and its coupling relationship with material composition: An integrated study of multiple experiments. *Mar. Pet. Geol.* **2022**, *140*, 105648.
23. Yang, F.; Ning, Z.; Wang, Q.; Liu, H. Pore structure of Cambrian shales from the Sichuan Basin in China and implications to gas storage. *Mar. Pet. Geol.* **2016**, *70*, 14–26. [CrossRef]
24. Zhu, H.; Ju, Y.; Qi, Y.; Huang, C.; Zhang, L. Impact of tectonism on pore type and pore structure evolution in organic-rich shale: Implications for gas storage and migration pathways in naturally deformed rocks. *Fuel* **2018**, *228*, 272–289. [CrossRef]
25. Wang, G.; Long, S.; Peng, Y.; Ju, Y. Characteristics of Organic Matter Particles and Organic Pores of Shale Gas Reservoirs: A Case Study of Longmaxi-Wufeng Shale, Eastern Sichuan Basin. *Minerals* **2020**, *10*, 137. [CrossRef]
26. Zhang, P.; Misch, D.; Hu, F.; Kostoglou, N.; Scahenhofer, R.F.; Liu, Z.; Meng, Q.; Bechtel, A. Porosity evolution in organic matter-rich shales (Qingshankou Fm.; Songliao Basin, NE China): Implications for shale oil retention. *Mar. Pet. Geol.* **2021**, *130*, 105319. [CrossRef]
27. Ma, C.; Zhao, X.; Yang, T.; Jiang, W.; Guo, B.; Han, G.; Bi, H.; Ma, J.; Bian, C.; Zhou, K.; et al. Mineralogy, organic geochemistry, and microstructural characterization of lacustrine Shahejie Formation, Qikou Sag, Bohai Bay Basin: Contribution to understanding microcosmic storage mechanism of shale oil. *J. Pet. Sci. Eng.* **2022**, *209*, 109843. [CrossRef]
28. Kelly, S.; El-Sobky, H.; Torres-Verdín, C.; Balhoff, M.T. Assessing the utility of FIB-SEM images for shale digital rock physics. *Adv. Water Resour.* **2016**, *95*, 302–316. [CrossRef]
29. Li, Z.; Liu, D.; Cai, Y.; Ranjith, P.; Yao, Y. Multi-scale quantitative characterization of 3-D pore-fracture networks in bituminous and anthracite coals using FIB-SEM tomography and X-ray μ-CT. *Fuel* **2017**, *209*, 43–53. [CrossRef]
30. Klaver, J.; Desbois, G.; Urai, J.L.; Littke, R. BIB-SEM study of the pore space morphology in early mature Posidonia Shale from the Hils area, Germany. *Int. J. Coal Geol.* **2012**, *103*, 12–25. [CrossRef]
31. Klaver, J.; Desbois, G.; Littke, R.; Urai, J.L. BIB-SEM characterization of pore space morphology and distribution in postmature to overmature samples from the Haynesville and Bossier Shales. *Mar. Pet. Geol.* **2015**, *59*, 451–466.
32. Klaver, J.; Desbois, G.; Littke, R.; Urai, J.L. BIB-SEM pore characterization of mature and post mature Posidonia Shale samples from the Hils area, Germany. *Int. J. Coal Geol.* **2016**, *158*, 78–89.
33. Zhang, P.; Lu, S.; Li, J.; Chang, X.; Li, J.; Li, W.; Chen, G.; Wang, S.; Feng, W. Broad ion beam-scanning electron microscopy pore microstructure and multifractal characterization of shale oil reservoir: A case sample from Dongying Sag, Bohai Bay Basin, China. *Energ. Explor. Exploit.* **2020**, *38*, 613–628. [CrossRef]
34. Jarvie, D.M. Shale resource systems for oil and gas; Part 1, Shale-gas resource systems. *AAPG Mem.* **2012**, *97*, 69–87.
35. Shi, M.; Yu, B.; Xue, Z.; Wu, J.; Yuan, Y. Pore characteristics of organic-rich shales with high thermal maturity: A case study of the Longmaxi gas shale reservoirs from well Yuye-1 in southeastern Chongqing, China. *J. Nat. Gas Sci. Eng.* **2015**, *26*, 948–959. [CrossRef]
36. Wang, S.; Li, J.; Lu, S.; Zhang, P.; Zhang, J.; Li, W. Development characteristics of organic matter pores of Marine shale in the Southeastern Chongqing, China. *J. Earth Sci. Envir.* **2019**, *41*, 721–733.
37. Wang, C.; Song, Y.; Li, Z.; Jiang, Z.; Zhou, C.; Chen, Z.; Chang, J.; Hong, L. Variation in the brittle-ductile transition of Longmaxi shale in the Sichuan Basin, China: The significance for shale gas exploration. *J. Pet. Sci. Eng.* **2022**, *209*, 109858.
38. Locks, R.G.; Reed, R.M.; Ruppel, S.C.; Hammes, U. Spectrum of pore types and networks in mudrocks and a descriptive classification for matrix-related mudrock pores. *AAPG Bull.* **2012**, *96*, 1071–1098. [CrossRef]
39. Liu, X.; Lai, J.; Fan, X.; Shu, H.; Wang, G.; Ma, X.; Liu, M.; Guan, M.; Luo, Y. Insights in the pore structure, fluid mobility and oiliness in oil shales of Paleogene Funing Formation in Subei Basin, China. *Mar. Pet. Geol.* **2020**, *114*, 104228. [CrossRef]
40. Xu, Y.; Lun, Z.; Pan, Z.; Wang, H.; Zhou, X.; Zhao, C.; Zhang, D. Occurrence space and state of shale oil: A review. *J. Pet. Sci. Eng.* **2022**, *211*, 110183. [CrossRef]
41. Wang, X.; Wang, M.; Li, J.; Shao, H.; Deng, Z.; Wu, Y. Thermal maturity: The controlling factor of wettability, pore structure, and oil content in the lacustrine Qingshankou shale, Songliao Basin. *J. Pet. Sci. Eng.* **2022**, *215*, 110618. [CrossRef]
42. Zhang, P.; Lu, S.; Li, J.; Zhang, J.; Xue, H.; Chen, C. Comparisons of SEM, Low-Field NMR, and Mercury Intrusion Capillary Pressure in Characterization of the Pore Size Distribution of Lacustrine Shale: A Case Study on the Dongying Depression, Bohai Bay Basin, China. *Energy Fuels* **2017**, *31*, 9232–9239. [CrossRef]
43. Chen, Q.; Zhang, J.; Tang, X.; Li, W.; Li, Z. Relationship between pore type and pore size of marine shale: An example from the Sinian–Cambrian formation, upper Yangtze region, South China. *Int. J. Coal Geol.* **2016**, *158*, 13–28. [CrossRef]

44. Wang, P.; Jiang, Z.; Ji, W.; Zhang, C.; Yuan, Y.; Chen, L.; Yin, L. Heterogeneity of intergranular, intraparticle and organic pores in Longmaxi shale in Sichuan Basin, South China: Evidence from SEM digital images and fractal and multifractal geometries. *Mar. Pet. Geol.* **2016**, *72*, 122–138. [CrossRef]
45. Münch, B.; Holzer, L. Contradicting Geometrical Concepts in Pore Size Analysis Attained with Electron Microscopy and Mercury Intrusion. *J. Am. Ceram. Soc.* **2008**, *12*, 4059–4067. [CrossRef]
46. Li, J.; Ma, Y.; Huang, K. Quantitative characterization of organic acid generation, decarboxylation, and dissolution in a shale reservoir and the corresponding applications—A case study of the Bohai Bay Basin. *Fuel* **2018**, *214*, 538–545. [CrossRef]
47. Zhang, P.; Lu, S.; Li, J. Characterization of pore size distributions of shale oil reservoirs: A case study from Dongying sag, Bohai Bay basin, China. *Mar. Pet. Geol.* **2019**, *100*, 297–308. [CrossRef]
48. Yao, Y.; Liu, D. Comparison of low-field NMR and mercury intrusion porosimetry in characterizing pore size distributions of coals. *Fuel* **2012**, *95*, 152–158. [CrossRef]
49. Lubelli, B.; de Winter, D.A.M.; Post, J.A.; van Hees, R.P.J.; Drury, M.R. Cryo-FIB–SEM and MIP study of porosity and pore size distribution of bentonite and kaolin at different moisture contents. *Appl. Clay Sci.* **2013**, *80–81*, 358–365. [CrossRef]